Growth and atomic geometry of bismuth and antimony on InP(110) studied using low-energy electron diffraction

W. K. Ford,* T. Guo,† and K.-J. Wan
Advanced Materials Center, Montana State University, Bozeman, Montana 59717
and Department of Physics, Montana State University, Bozeman, Montana 59717

C. B. Duke
Xerox Webster Research Center, 800 Phillips Road, 0114-38D, Webster, New York 14580
(Received 9 October 1991)

Low-energy electron-diffraction (LEED) intensities are reported for 17 or 18 symmetry-inequivalent beams of normally incident electrons diffracted from InP(110), InP(110)-$p(1\times1)$-Sb (1 monolayer), and InP(110)-$p(1\times1)$-Bi (1 monolayer). These intensities were obtained over an energy range 40 eV $\leq E \leq 300$ eV for samples at $T=120$ K. Structural determinations are given for all three systems, based on comparing the calculated and measured diffracted intensities using x-ray R factors as measures of the quality of the description of the measured intensities. The InP(110) surface exhibits a nearly bond-length-conserving top-layer rotational relaxation characterized by a tilt angle of $\omega=31°$ with the P species displaced outward from the surface and the In inwards, in accord with prior structure analyses of this surface. Adsorption of either Sb or Bi removes this relaxation, with the adsorbed species forming chains with atoms near the positions which were occupied by In and P in the clean surface (i.e., the "epitaxical continued layer structure"). The adsorbed atom bonded to the In top-layer substrate species is slightly displaced outwards from the surface, giving a top-layer tilt angle of $\omega=4°$ for Sb and $\omega=5°$ for Bi. Bond lengths are approximtely those expected for covalent bonds between adsorbates and between the adsorbates and substrate species. The adsorbate-adsorbate bond is lengthened by 1–2%, the adsorbate-phosphorus bond by about 2%, and the adsorbate-indium bond is shortened by 1% or less.

I. INTRODUCTION

The monolayer growth of antimony on III-V (110) semiconductor substrates has been the subject of many previous studies.[1–25] Interest has been mostly focused on its formation of an epitaxical monolayer,[1–4] its status as a precursor to the formation of a metal-semiconductor contact,[5,13–19] and its exhibition of a unique type of surface chemical bond as reflected by the occupied surface states evident in angle-dependent photoemission spectra.[6–12] Recent reviews of most of this work may be found in the literature.[26–28]

Recently, however, more general interest in column-V-atom adsorption on III-V (110) interfaces has emerged following the discovery that bismuth also forms ordered thin films on many III-V (110) substrates.[29–51] These are among the rare illustrations of metal–III-V-semiconductor interfaces with two-dimensional crystalline order. Consequently, they constitute valuable prototypes for studies of the formation and properties of idealized metal-semiconductor heterojunctions.[6,20,52] Of specific value is the small unit cell of the zinc-blende-structure (110) surface which renders tractable detailed theoretical calculations of geometry and electronic structure. Hence these systems can be used to develop insight and understanding of the correlation between atomic structure and electronic properties of metal-semiconductor interfaces. The determination of an accurate, detailed surface atomic geometry is the first step in such a process.

One might expect antimony and bismuth to chemisorb differently on the surface of tetrahedral semiconductors as reflected in different surface geometries. Antimony and bismuth are isovalent and form trigonal, nearly p^3 cubic semimetals as pure elements. However, each element bonds differently to other elements. Whereas bismuth is found most commonly in p^3-bonded compounds and is not known to form tetrahedral compounds, antimony commonly forms tetrahedral sp^3 bonds in tetrahedrally coordinated compound semiconductors, e.g., InSb and GaSb.[53] Nevertheless, Sb and Bi have been shown to exhibit analogous atomic geometries when chemisorbed epitaxically on GaAs(110).[2,42,45] It is of some interest, therefore, to contrast the behavior of antimony and bismuth bonding to a different common substrate, such as InP(110), on which antimony and bismuth both form ordered epitaxical monolayers.

InP(110) was selected for study for two reasons: First, it is the second known example where the antimony and bismuth adsorbates form ordered structures on a III-V (110) substrate yielding a (1×1) low-energy electron-diffraction (LEED) pattern.[38] Second, InP has a slightly larger unit cell than GaAs. LEED (Refs. 39–42 and 45) and scanning tunneling microscopy (STM) (Refs. 32, 34, and 35) studies of the Bi/GaAs(110) system indicate that at one monolayer (ML) coverage the zigzag chain structure is punctuated by vacancies every six unit cells, giving rise to a (6×1) symmetry. The vacancy defects occur to

relieve the surface strain which results from a lattice mismatch between the bismuth overlayer and substrate periodicity. Since the InP(110) surface unit cell is larger than that of GaAs(110) by approximately 6%, reduced surface strain is expected, which would serve to diminish the hypothesized driving force for a superlattice reconstruction. Thus the study of the Bi/InP(110) system provides an opportunity to scrutinize the role of atomic size in epitaxical growth of such strained interfaces.[20]

In this paper we present the results of LEED studies of the growth characteristics and atomic structure of the Bi/InP(110) interface. A semiquantitative analysis of the diffraction-intensity profiles and spot angular profiles is performed to illustrate the ordering properties. We show that upon deposition of one monolayer of bismuth the adatoms form a well-defined $p(1\times1)$ overlayer. The growth of bismuth is two dimensional for the first monolayer, beyond which it is three dimensional and disordered. For submonolayer coverages bismuth adatoms form monoatomic terraces, which tend to be distributed periodically in the $[1\bar{1}0]$ direction. In addition, a dynamical LEED-intensity analysis was performed to determine a detailed geometry of the InP(110)-$p(1\times1)$-Bi(1 ML) phase. Two major classes of geometric models were examined. The first model is the epitaxical continued-layer structure (ECLS) depicted in Fig. 1. This geometry provides the best-fit LEED prediction for the related 1-ML

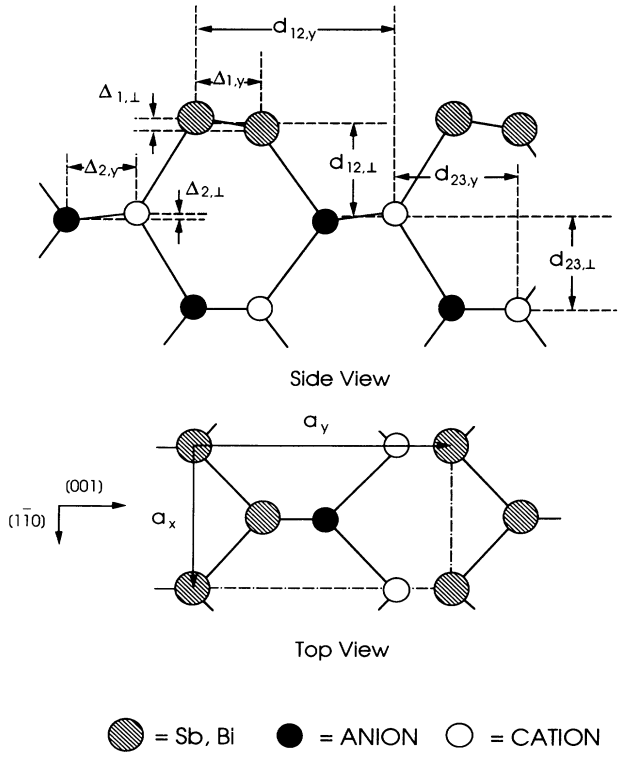

FIG. 1. Schematic drawing of the epitaxical continued-layer structure (ECLS) depicting Sb or Bi bonded to a zinc-blende-structure (110) substrate. The first- and second-layer shear angles are given as $\omega_i = \arctan(\Delta_{i,\perp}/\Delta_{i,y})$ for $i=1,2$. A negative ω_i and a positive ω_2 are depicted in the drawing.

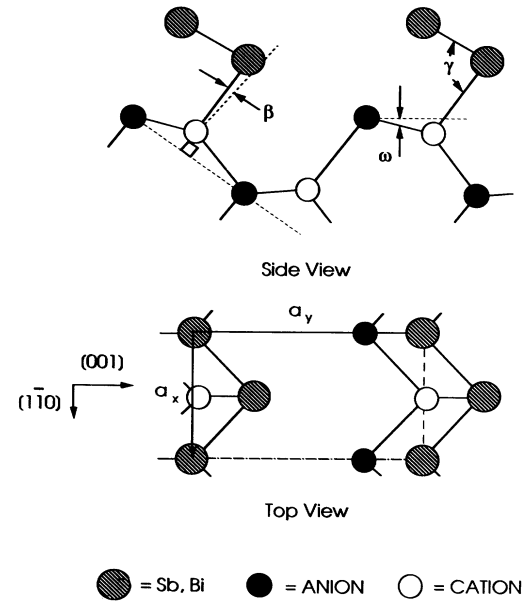

FIG. 2. Schematic drawing of the epitaxical on-top structure (EOTS) depicting Sb or Bi bonded to a zinc-blende-structure (110) substrate. β is positive, ω is negative, and $\gamma \approx \pi/2$, as depicted in the drawing.

structures exhibited by Sb/GaAs(110), Sb/InP(110), and Bi/GaAs(110).[2,9,42,45] The second model is the relaxed Skeath or epitaxical on-top structure (EOTS) depicted in Fig. 2. This geometry has been proposed from interpretations of photoemission and STM data[1,17] and from total-energy calculations[20] as a possible alternative to the ECLS for Sb/III-V (110) interface systems. LEED-intensity data also were collected and analyzed for the clean InP(110) and InP(110)-$p(1\times1)$-Sb(1 ML) systems. By analyzing these previously studied[7–9] systems and comparing them with the bismuth overlayer system, a single, self-consistent combined theoretical and experimental description of the antimony and bismuth adsorption has been developed.

We proceed by describing the acquisition of the experimental data and the calculation of the model LEED intensities in Sec. II. The results of our structural analysis are presented in Sec. III and discussed in Sec. IV. The paper concludes with a synopsis.

II. METHODS

A. Experimental procedures

The InP(110) substrates were prepared by cleaving *in situ* InP *n*-type bars using techniques described previously.[40] Bismuth and antimony were deposited by sublimination from the bulk of high-purity (99.9999%) material at a typical rate of less than 1 Å/min. The evaporation pressure during the sublimination was always less than 4×10^{-10} Torr, and the substrates were held far from the source to minimize radiant heating. One monolayer is defined according to the surface atomic density of the InP(110) substrate, 8.2×10^{14} atoms/cm^2, i.e., two ada-

toms per substrate-surface unit cell. The film thicknesses were measured using a quartz-crystal oscillator (QCO) thin-film monitor.[40] The QCO thin-film monitor was positioned in close proximity to the InP substrate to monitor the deposition during the evaporation. Auger measurements, performed using the retarding-field technique and LEED grids, and were used to verify surface coverages.

The LEED measurements were made using a video-based instrument.[40] The resolving capacity, or minimum angle of resolution of the diffractometer, has been determined to be better than 0.33°. For the spot-profile measurements reported in this paper, one data point (i.e., video-screen pixel) corresponds to a subtended angle of about 0.26°. The diffraction intensities were collected for normal-incidence electrons from digitized and integrated LEED images, summed typically over 32 video frames. The measurement of a set of 17 or more intensity–versus–kinetic-energy profiles, collected in 2-eV increments from 40 to 300 eV, was made within minutes. The resulting data were averaged over repeated measurements and over symmetry-equivalent beams and then normalized to the incident-beam current. The incident-beam current varied with beam energy in a range 0.3–2.5 μA. All intensity profiles used in the structure determination were measured at low temperature, typically 120 K, to minimize the Debye-Waller scattering component of the diffraction beam. The annealing of the monolayer Bi and Sb films after deposition resulted in no change in the intensity profiles. Thus annealing was not performed for films used for the structure determination.

B. Calculations

A dynamical multiple-scattering model was used to analyze the experimental intensity profiles.[54,55] This model is constructed following the multiple-scattering formalism of Duke and co-workers[56–59] and Beeby[60] in which energy-dependent scattering phase shifts and an energy-dependent electron inelastic mean free path are utilized. The details of the model calculations have been summarized elsewhere.[45] We show in Fig. 3 the phase shifts employed for each atom in the calculation. These phase shifts were computed for neutral atoms. The atomic po-

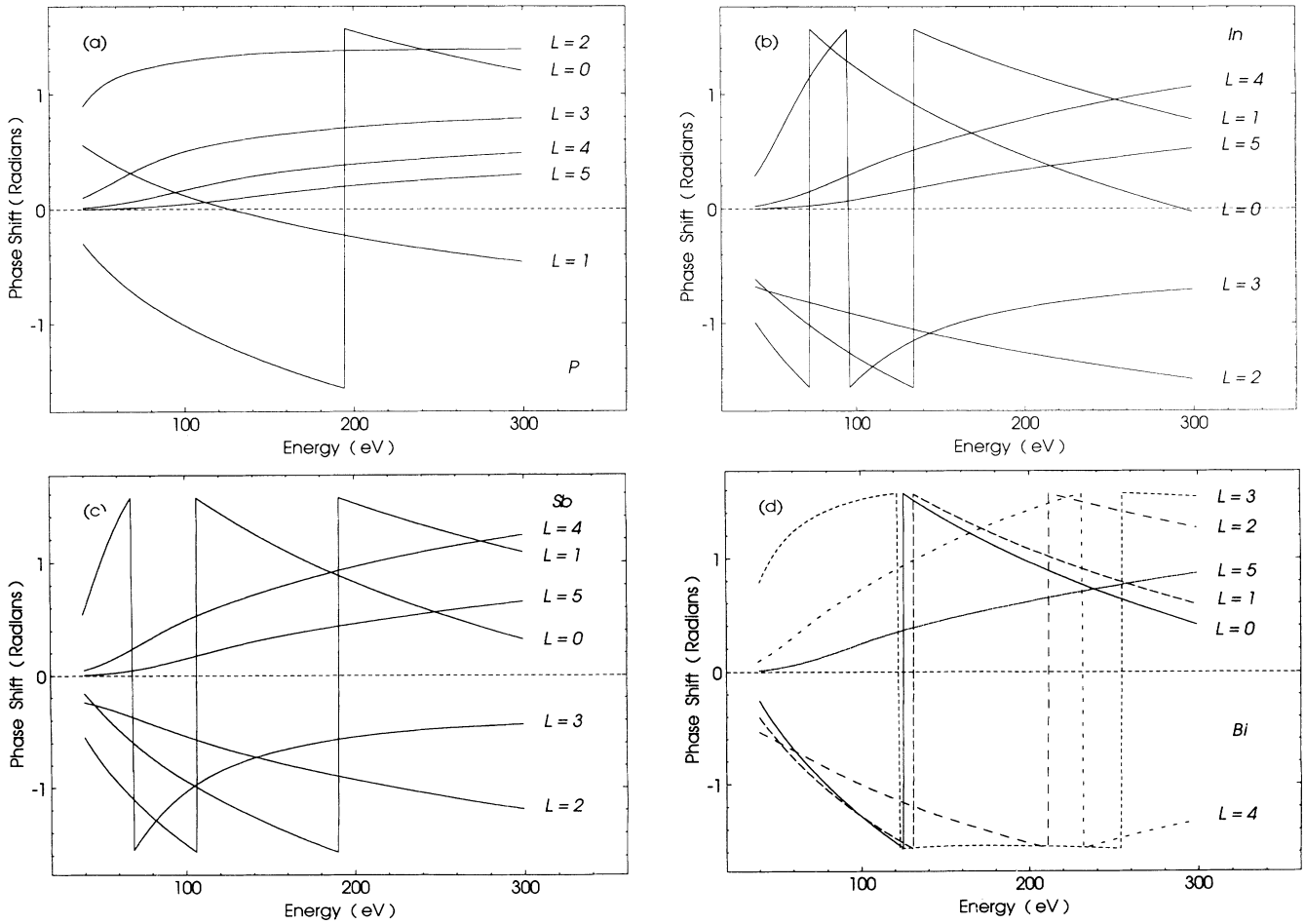

FIG. 3. Energy-dependent phase shifts used in the theoretical calculations: (a) phosphorus, (b) indium, (c) antimony, and (d) bismuth. The relativistic Hartree-Fock-Slater model with energy-dependent Hara exchange potentials is used to obtain these phase shifts.

tentials for the In and P atoms were computed by averaging charge densities over the nearest 16 shells of atoms in the bulk. Those for the adsorbates were computed without charge-density averaging. The potentials were evaluated using the relativistic Hartree-Fock-Slater model and Hara energy-dependent exchange.[58,59] Phase shifts are obtained from a muffin-tin approximation to the calculated potentials. The total elastic-scattering cross sections for each atom are compared in Fig. 4. Note the dominance of the bismuth cross sections over those of the other atoms throughout the entire energy range.

A structure determination is accomplished by comparing the experimental intensity profiles with multiple-scattering simulations for a sequence of trial atomic geometries. In the work reported herein, each geometry is specified by a set of bond lengths and bond angles (Figs. 1 and 2) and two nonstructural parameters: the real and imaginary parts of the inner potential. In the computer code, the search of parameter values has been automated using the simplex nonlinear optimization algorithm and x-ray reliability factor R_x as the figure of merit.[45,61]

The structure searches were performed in three steps.[45] First, an optimal geometry was found by varying the bond angles and inner potential values while keeping the bond lengths between the atoms fixed. Specifically, the bulk nearest-neighbor spacings were selected as the substrate bond lengths, an the covalent bond lengths were selected for the overlayer bonds. The first step was repeated for different starting conditions if the first attempt did not lead to R_x values of less than approximately 0.3. In the second step, the bond lengths were allowed to vary within approximately 20% of their covalent values together with the other model parameters. The second step was also repeated if the R_x values were too large, near to 0.3, or to ensure that the structure predicted represented a global minimum. Finally, the best-fit values were obtained by varying each parameter individually about the value obtained at the end of the simplex search. This procedure differs significantly from that used by other workers[54,55] in that refinements in the bond lengths involve variations in the atomic coordinates normal to the surface (e.g., $\Delta_{1,\perp}$ and $d_{12,\perp}$). Since these coordinates are precisely determined by LEED, the bond lengths appear to be determined with comparable precision. Displacements parallel to the surfaces are not so precisely specified, however, so the uncertainties in the bond lengths are larger than those we obtain from our use of bond lengths as the independent structural variables.

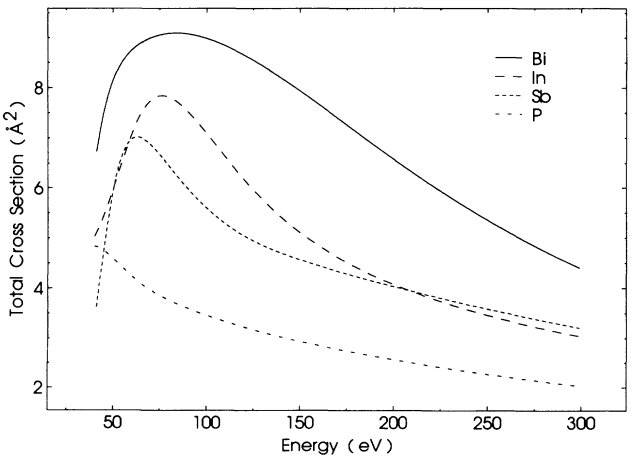

FIG. 4. Total elastic cross sections of indium, phosphorus, antimony, and bismuth computed from the phase shifts shown in Fig. 3 and plotted as a function of incident-beam energy.

III. RESULTS

A. InP(110)

Intensity profiles were collected from clean InP(110) to check our experimental conditions relative to those of previous workers.[54,55] Thirty beams consisting of 18 symmetry-inequivalent beams were measured over the 40–300-eV energy range. These data are plotted in Fig. 5 in which the relative intensities within each panel have been retained. The most intense beams are depicted in Fig. 5(a), and the least intense ones are in Fig. 5(c). The intensity grouping in Fig. 5 was obtained by integrating the data over the indicated energy range. Our visual comparison of the experimental intensity profiles in Fig. 5 to those published by Meyer *et al.*[54] indicates excellent agreement. The results of our multiple-scattering calculations for InP(110) are listed in Table I, and the computed intensity profiles corresponding to the best-fit geometry are plotted in Fig. 5 together with the experimental data. Because the geometry of InP(110) has previously been well established,[55] only the clean-surface version of the ECLS geometry, in which the overlayer atoms in Fig. 1 are replaced by the corresponding In and P atoms, was tested. In the tables,

$$\omega_i = \tan^{-1}(\Delta_{i,\perp}/\Delta_{i,\parallel}) \quad (1)$$

designate the tilt angles of the chains of atoms in the layer designated by i relative to the unrelaxed InP(110) surface. Positive values of ω_i correspond to cations displaced outward and anions inward.

Four sets of results for clean InP(110) are given in Table I. To obtain the first two entries, the calculations were performed using five and six phase shifts in the scattering model and keeping the bond lengths fixed at the bulk nearest-neighbor values of 2.54 Å during the search (as described above). The six-phase-shift best-fit geometry, specified as the third entry, was obtained by relaxing the fixed-bond-length constraint and refining the optimum geometry that results, as described in Sec. II B. The seven-phase-shift values are the result of a full seven-parameter search about the best-fit six-phase-shift structure. The results of these calculations indicate that although the R_x values change considerably between the first three cases, the five-phase-shift representation is adequate for determining a reliable geometry for the clean InP(110) surface. Only subtle changes in the details of the best-fit structure result when additional phase shifts are used. The six- and seven-phase-shift calculations are

believed to yield structures whose determination as a function of the number of phase shifts has converged.

B. InP(110)-$p(1\times1)$-Sb

A characterization of the growth and atomic geometry of Sb on InP(110) was revisited in the present study to extend the previous LEED analysis of this system[8,9] to include a consideration of the EOTS geometry (cf. Fig. 2) and to provide a reference for use in our Bi/InP(110) studies. The LEED intensities exhibit distinct variations in all beams as a function of increasing Sb deposition. Generally, the beam intensities initially diminish, and the peak positions shift with increasing Sb coverage. Near the completion of one monolayer coverage, however, the intensities increase and the peak positions stop changing. For coverages greater than 1 ML, the intensities resume their decline in relation to the background intensities, but no additional changes in the intensity profiles are observed.

The nine lowest-order diffraction-beam intensities are compared in Fig. 6 with the corresponding beams for the clean surface as a function of Sb coverage using the x-ray reliability factor R_x. A continuous charge in R_x occurs

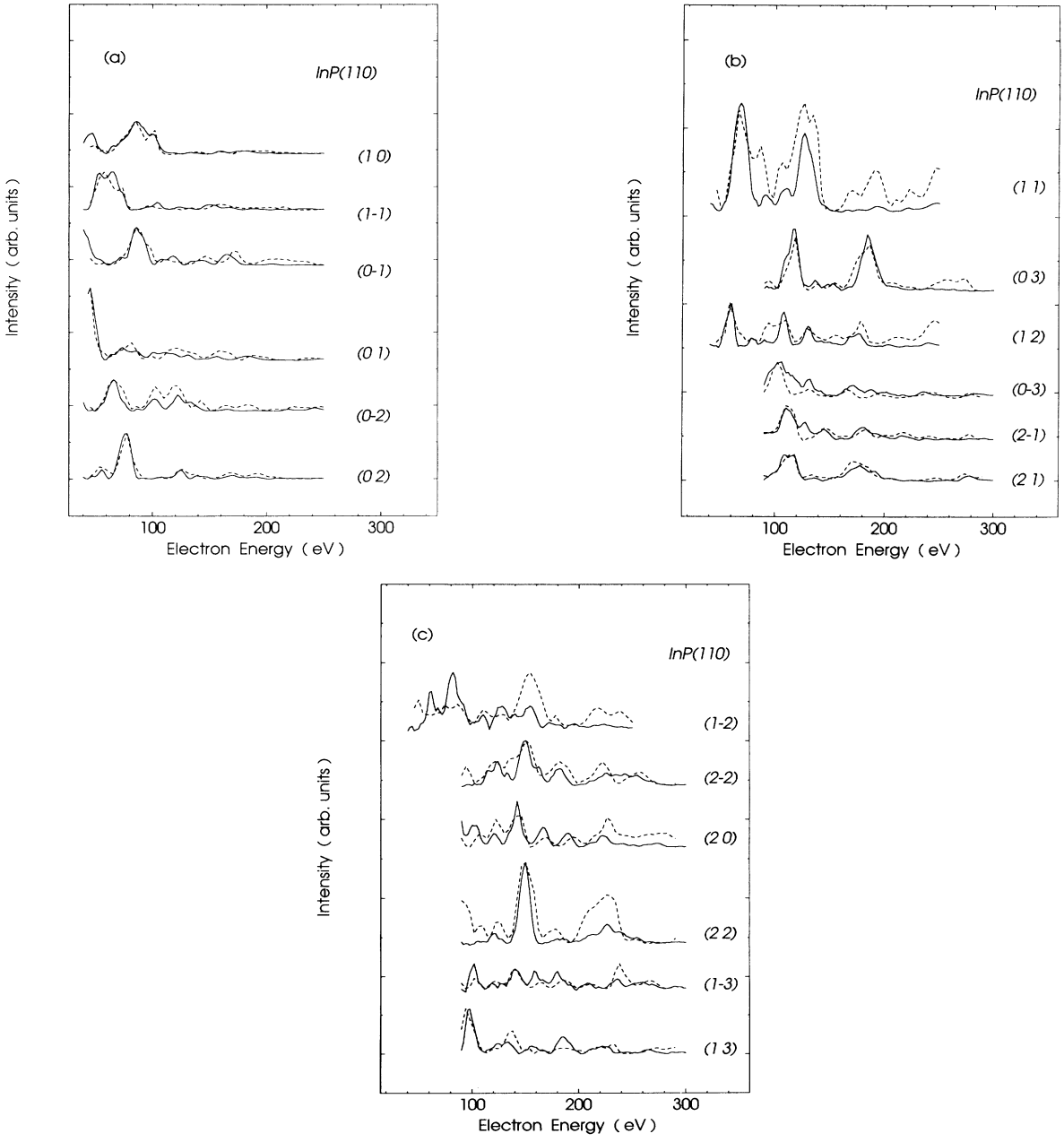

FIG. 5. Measured LEED-intensity profiles for InP(110) (solid curves), grouped according to integrated beam intensities: (a) strongest, (b) medium, and (c) weakest. The relative intensities of the beams are retained within each panel. The dashed lines indicate the computed intensities of the best-fit structural model listed in Table I.

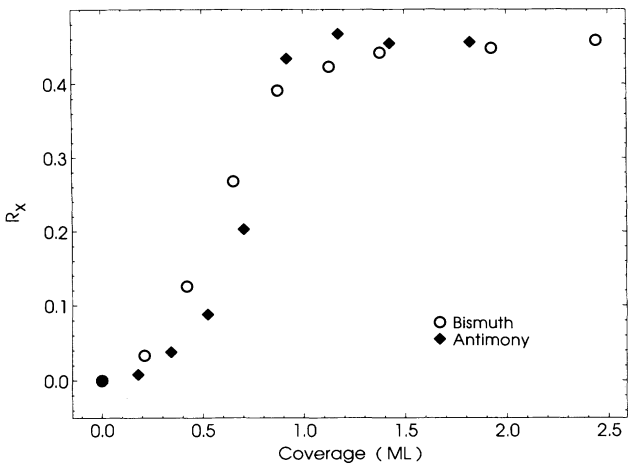

FIG. 6. Variation of the x-ray r factor R_x, with coverage for Sb and Bi on InP(110), calculated comparing the intensity profiles of the epitaxial overlayers with those of clean InP(110). R_x is computed for the nine lowest-order diffraction beams. The diamonds denote Sb data, and the circles represent Bi data.

up to 1 ML, but ceases for greater coverages. The lack of change at greater coverages suggests that no further modification in the long-range order is occurring and that two-dimensionally disordered differential absorption is beginning. This conclusion is consistent with previous, more qualitative descriptions of the growth of Sb on InP(110).[8]

In Fig. 7 the intensity profiles for the set of 17 unique, symmetry-averaged diffraction beams measured for InP(110)-$p(1\times1)$-Sb(1 ML) are presented, grouped in order of integrated intensity as in Fig. 5. Three geometric models of InP(110)-$p(1\times1)$-Sb(1 ML) were considered in the analysis of these data: the ECLS, the disordered structure, and the EOTS. The results of our multiple-scattering calculations are presented in Table I for the ECLS geometry and in Table II for the disordered geometry. For the latter case, it was assumed that the Sb atoms form a disordered overlayer on top of the substrate and thus do not directly contribute to the diffraction, although bond angles and inelastic-scattering mechanisms of the ordered substrate may change. Accordingly, the InP(110)-$p(1\times1)$-Sb(1 ML) intensity profiles were calculated as though the surface was "clean," using the ECLS geometry with fixed bond lengths, but without including any Sb scattering. Only six phase shifts were used in the disordered-model calculations.

Our best results using the third structural model, the EOTS geometry, are specified in Table III. Both fixed- and variable-bond-length searches were performed and values of γ near 60° and 90° were considered (cf. Fig. 2). The EOTS model never led to a good description of the

TABLE I. Results of the dynamical LEED-intensity analysis for the epitaxical continued-layer structure (ECLS) model (cf. Fig. 1). The quantity ω_1 designates the tilt angle of the layer labeled by i relative to the reconstructed InP(110) surface. $(C)_i$-$(A)_j$ corresponds to the bond length between the atom in the cation position of layer i and the atom in the anion position of layer j. V_0 and V_1 refer to the real and imaginary parts of the inner potential.

ECLS model	ω_1 (deg)	$(C)_2$-$(A)_1$ (Å)	$(C)_1$-$(A)_1$ (Å)	$(C)_1$-$(A)_2$ (Å)	ω_2 (deg)	V_0 (eV)	V_1 (eV)	R_x
InP(110)								
Fixed bond length, five phase shifts	−30.6	2.54	2.54	2.54	1.4	8.6	4.7	0.216
Fixed bond length, six phase shifts	−29.4	2.54	2.54	2.54	0.2	8.4	4.6	0.183
Best fit, six phase shifts	−30.8	2.54	2.51	2.50	0.5	9.0	4.6	0.168
Best fit, seven phase shifts	−31.1	2.55	2.52	2.49	0.5	8.5	4.5	0.163
Sb/InP(110)								
Fixed bond length, six phase shifts	−6.5	2.84	2.80	2.46	0.4	9.6	4.1	0.264
Best fit, six phase shifts	−4.7	2.84	2.81	2.54	0.3	8.6	4.6	0.250
Best fit, seven phase shifts	−3.9	2.80	2.82	2.52	1.1	8.5	4.5	0.241
Bi/InP(110)								
Fixed bond length, six phase shifts	−4.4	2.90	2.92	2.52	−2.7	10.1	3.7	0.294
Best fit, six phase shifts	−3.9	2.88	3.02	2.55	−2.6	9.7	3.9	0.287
Best fit, seven phase shifts	−5.4	2.88	2.98	2.58	−1.5	9.4	4.0	0.254

TABLE II. Results of the dynamical LEED-intensity analysis for the disordered overlayer structural model. Six phase shifts were used in the model calculations. The symbols in the table are defined in the caption to Table I.

Disordered model	ω_1 (deg)	$(C)_2$-$(A)_1$ (Å)	$(C)_1$-$(A)_1$ (Å)	$(C)_1$-$(A)_2$ (Å)	ω_2 (deg)	V_0 (eV)	V_1 (eV)	R_x
Sb/InP(110)								
Fixed bond length	0.5	2.54	2.54	2.54	2.3	8.8	4.8	0.283
Bi/InP(110)								
Trial 1	4.8	2.54	2.54	2.54	2.0	7.7	5.7	0.387
Trial 2	29.3	2.54	2.54	2.54	1.6	9.6	5.1	0.374

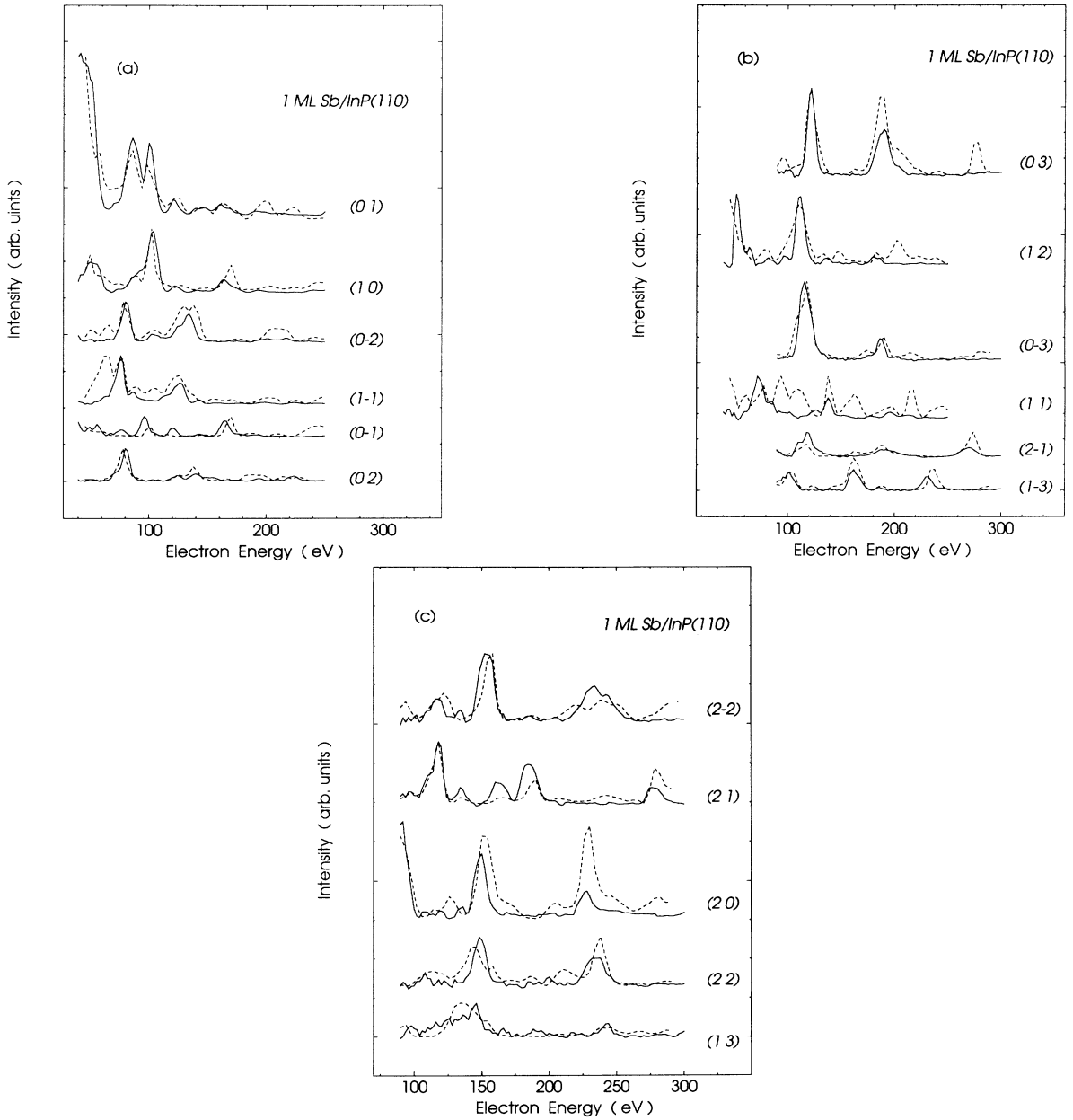

FIG. 7. Measured LEED-intensity profiles for InP(110)-$p(1\times1)$-Sb(1 ML) (solid curves), grouped according to integrated beam intensities: (a) strongest, (b) medium, and (c) weakest. The relative intensities of the beams are retained within each panel. The dashed lines are the computed intensities of the best-fit structural model listed in Table I.

TABLE III. Results of the dynamical LEED-intensity analysis for the epitaxical on-top structure (EOTS) model (cf. Fig. 2). Symbols in the table are defined in Fig. 2 and the caption to Table I.

EOTS model	γ (deg)	β (deg)	$(C)_2$-$(A)_1$ (Å)	$(C)_1$-$(A)_1$ (Å)	ω_1 (deg)	V_0 (eV)	V_1 (eV)	R_x
Sb/InP(110)								
Fixed bond lengths	52.6	0.9	2.84	2.80	3.3	10.5	2.8	0.334
Bi/InP(110)								
Fixed bond lengths Trial 1	60.5	−11.2	2.90	2.92	−30.8	10.5	2.9	0.413
Fixed bond lengths Trial 2	57.0	−1.3	2.90	2.92	−6.7	9.6	3.9	0.440
Variable bond lengths	49.3	−4.7	2.92	2.91	−2.6	9.9	3.9	0.430

measured intensities. Furthermore, the precise geometry obtained at the end of the search depended on the starting structure. These two results lead us to conclude that the EOTS model is not consistent with the LEED-intensity data. Overall, the ECLS geometry provides the most probable structure of the InP(110)-$p(1\times1)$-Sb(1 ML) system, in agreement with the conclusion of previous workers.[9] The intensity profiles computed for InP(110)-$p(1\times1)$-Sb(1 ML) using the best-fit parameters listed in Table I and seven phase shifts in the model are plotted together with the experimental data in Fig. 7.

C. InP(110)-$p(1\times1)$-Bi

As in the case of Sb, the LEED intensities from Bi on InP(110) changed continuously with increasing Bi coverage. The aggregate change in the diffraction intensities is indicated in Fig. 6 where the intensity profiles of the nine lowest-order beams for room-temperature-prepared films are compared with the corresponding clean-surface InP(110) data using R_x as the figure of merit. Figure 6 indicates that the geometry changes continuously up to approximately 1 ML and that the Sb and Bi systems have essentially identical trends. The lack of additional changes at higher coverages indicates that subsequent Bi coverage does not order two dimensionally. It should be noted that the $(hk)=(\bar{h}k)$ symmetry of the clean InP(110) surface was observed for both Bi/InP and Sb/InP for all coverages studied. This symmetry corresponds to a reflection symmetry in the $[1\bar{1}0]$ direction of the surface. Incoherent scattering from the disordered overlayer noticeably increased the background of the diffraction pattern in both cases at coverages much below or above one monolayer.

For suitable systems the LEED spot angular profiles are replete with information about the formation of surface islands and steps.[62] In the present study, two-dimensional LEED patterns were measured for various bismuth coverages and electron energies. At submonolayer bismuth coverages, spot broadening was observed at certain energies. Energy-dependent angular-profile broadening also has been observed in other column-V/III-V (110) systems and was related to the formation of ordered two-dimensional islands.[4,8,38,41,43,45] The broadened spots split into satellites along the $[1\bar{1}0]$ direction, the orientation of the substrate zigzag chain (cf. Fig. 1). For illustration photographs of the LEED patterns at 69 eV for three coverages of Bi on InP(110) are presented in Fig. 8. Broadening and splitting of the diffracted beams are observed only at certain incident electron energies, which are different for different beams. The extra spots are not present for the clean surface prior to Bi deposition, which indicates that they are not due to surface defects or steps that may be caused by cleaving.

The variation of the angular spot profile with increasing Bi coverage was quantified by profiling the digitized

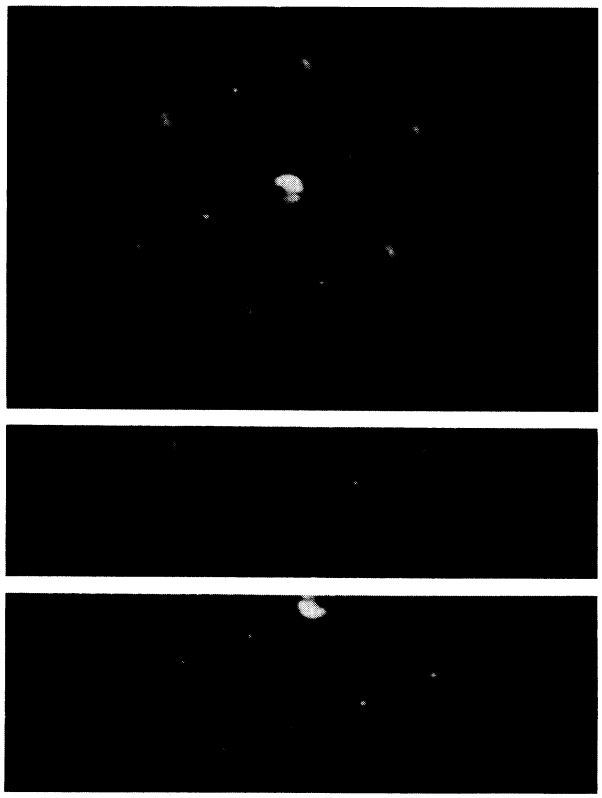

FIG. 8. LEED patterns at 69 eV for Bi/InP(110) for (a) 0.36 ML, (b) 0.55 ML, and (c) 0.96 ML.

LEED pattern along both [001] and [1$\bar{1}$0] directions: The profile of the (01) beam at 69 eV is presented in Fig. 9. The [1$\bar{1}$0] splitting that occurs is seen clearly at low coverage and disappears at coverages near one monolayer. The measured full width at half maximum (FWHM) and the separation of extra spots varies with increasing Bi coverage. In these measurements a typical unbroadened diffraction spot contains about 14 data points.

Finally, the symmetry-averaged intensity profiles for

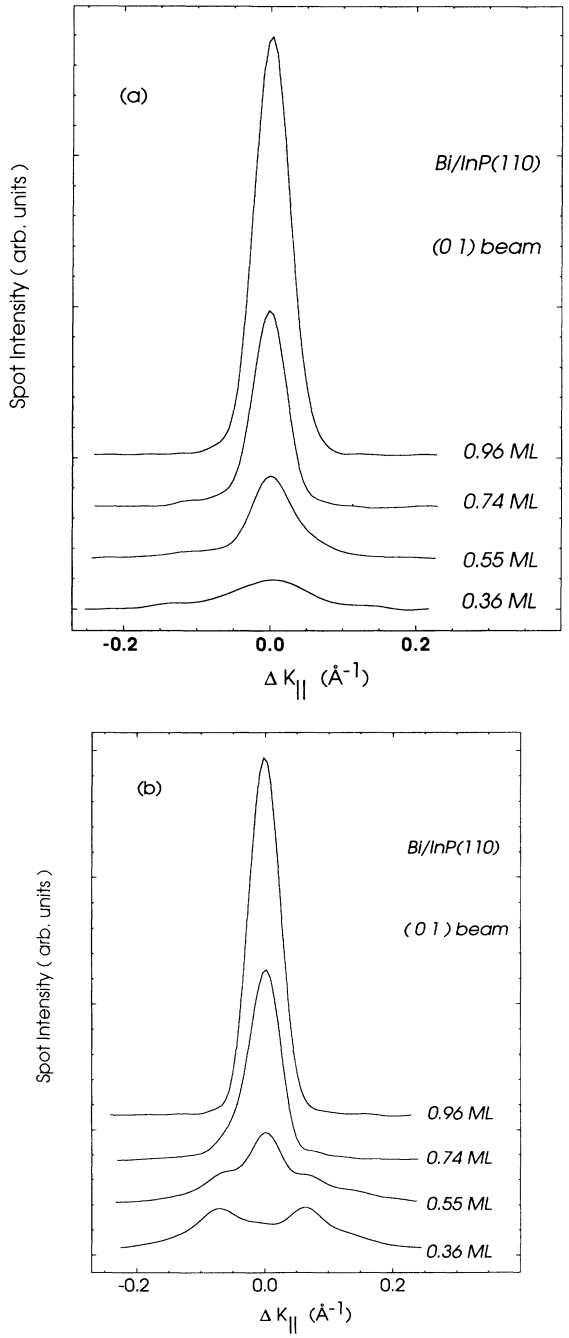

FIG. 9. LEED angular profiles for the 01 beam of Bi/InP(110) as a function of Bi coverage: (a) profile along the [001] direction and (b) profile along the [1$\bar{1}$0] direction.

InP(110)-$p(1\times1)$-Bi(1 ML) are presented and compared with the best-fit calculated intensity profiles in Fig. 10. As in Figs. 5 and 7, the beams are grouped in order of decreasing integrated intensity. The three structural models studied for Sb on InP(110) also were used for the analysis of the Bi data. The results of our multiple-scattering calculations are presented in Table I for the ECLS geometry, in Table II for the disordered geometry, and in Table III for the relaxed EOTS geometry. As for the Sb/InP calculations, both fixed- and variable-bond-length searches were performed and values of γ near 60° and 90° were considered for the EOTS model. Again, we observe that the converged parameters of the EOTS model depend on the initial simplex used and that the R_x values are always unacceptably large. Therefore we conclude that the EOTS model is inconsistent with the LEED-intensity profiles for InP(110)-$p(1\times1)$-Bi(1 ML) as well as for InP(110)-$p(1\times1)$-Sb(1 ML). The disordered model is eliminated for the same reasons. The two calculations listed in Table II for InP(110)-$p(1\times1)$-Bi(1 ML) correspond to the converged values for the disordered model computed using two different starting conditions in the search. The resultant geometries are quite different, and the R_x values indicate a poor fit. In contrast, the results presented in Table I for the ECLS model indicate a good description of the measurements by the calculated intensity profiles. The best-fit geometry is stable upon changes in the starting conditions in the search.

To attain an acceptably small value of R_x, seven phase shifts must be used in the calculations for the Bi system. In the Sb case, the use of seven phase shifts primarily modify the ω_1 and $(\mathrm{In})_2(\mathrm{Sb})_1$ parameters. In the Bi case, ω_1 and the $(\mathrm{Bi})_1(\mathrm{P})_2$ bond lengths are the most affected parameters. The need for seven phase shifts to describe the diffraction from a surface containing In and Sb or Bi is evident from Figs. 3 and 4. The heavier atoms have more nonvanishing terms in their partial-wave expansions, and additional terms are needed to describe adequately the differences between similar atoms. The greatest effect of including more partial waves can be seen in Table I for the Bi calculations.

IV. DISCUSSION

InP(110) is known[54,55] to undergo a reconstruction relative to the bulk-terminated geometry involving a rotation of approximately 30° by the surface InP chains (cf. Fig. 1). The same rotation is known to occur for all III-V (110) and II-VI (110) surfaces.[55] The driving force for the reconstruction is the rehybridization of the anion and cation into distorted p^3 and sp^2 local bonding configurations, respectively.[55]

In the best-fit InP(110) geometry determined here (cf. Table I), the rotation angle ω_1 is determined to be 31.1°. This value is close to the 30° value obtained previously.[54,55] Figure 11 shows the values of R_x obtained via the simplex method for fixed values of ω_1. One well-defined minimum in R_x occurs. No evidence exists for a secondary minimum near $\omega_1=0°$. This result differs from the earlier LEED analyses of the InP(110) system[55] because of our use of an automated-structure-search methodology

to obtain an optimum geometry for each fixed value of ω_1, the use of R_x as the sole criterion for the best fit, and the selection of the independent structural variables used in the fitting procedure.

The precise character of the more subtle geometrical changes are less certain. In Table IV we list the best-fit geometry determined here and contrast it to the results of previous model predictions[63,64] and experimental determinations[54,55,65,66] of the tilt angle ω_1, the interlayer separation $d_{12,\perp}$, and the bond lengths. The agreement among these values is fairly good. The extend x-ray-absorption fine-structure (EXAFS) measurement[65,66] of the top-layer InP bond appears to be inconsistent with the present LEED and theoretical tight-binding values, but the discrepancy is not significant. The EXAFS values are accurate only to ± 0.04 Å (Ref. 66) and the LEED values to ± 0.1 Å at best, given the large uncertainties of displacements parallel to the surface.[55] The best-fit geometry in Table IV displays a 9% contraction of the interplanar spacing relative to the bulk 2.075 Å. The contractions in the bond lengths are 2.0%, 0.8%, and -0.3% for the $(In)_1$-$(P)_2$, $(In)_1$-$(P)_1$, and $(In)_2$-$(P)_1$ bonds, respectively.

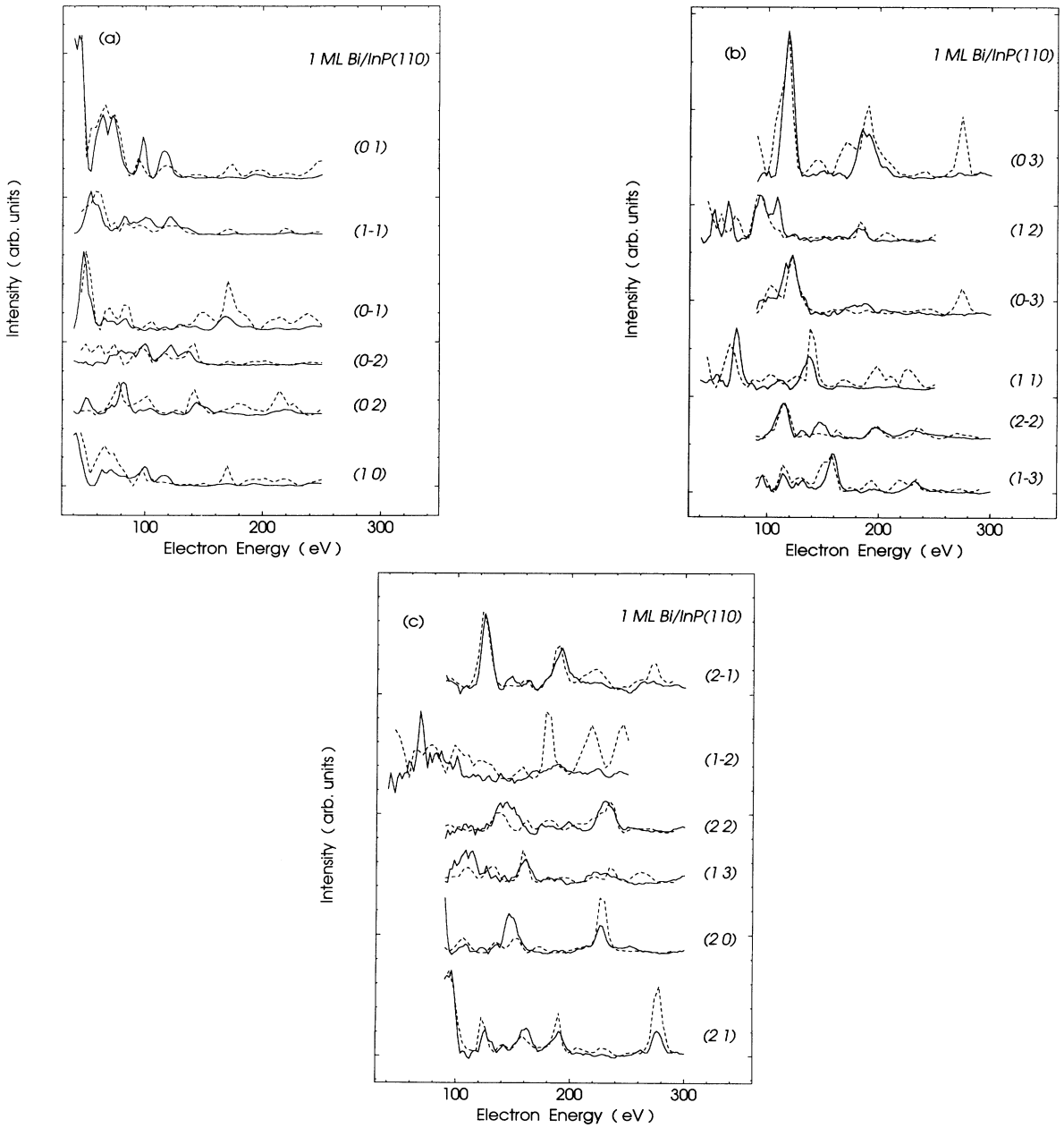

FIG. 10. Measured LEED-intensity profiles for InP(110)-$p(1\times1)$-Bi(1 ML) (solid curves), grouped according to integrated beam intensities: (a) strongest, (b) medium, and (c) weakest. The relative intensities of the beams are retained within each panel. The dashed lines are the computed intensities of the best-fit structural model listed in Table I.

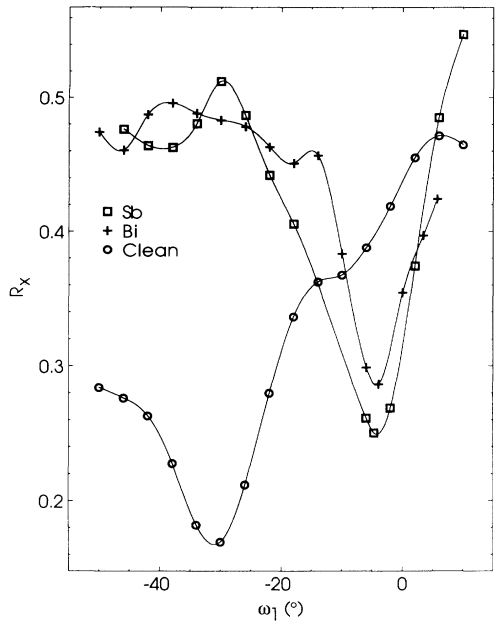

FIG. 11. R_x variation with top-layer shear angle ω_1 for three surfaces: InP(110), InP(110)-$p(1\times1)$-Sb(1 ML), and InP(110)-$p(1\times1)$-Bi(1 ML).

For comparison the parameters determined for GaAs(110), using the same procedure as employed here, are an 8% contraction of the interlayer spacing and contractions of 2.7%, −1.3%, and 1.1% for the $(Ga)_1$-$(As)_2$, $(Ga)_1$-$(As)_1$, and $(Ga)_1$-$(As)_2$ bonds, respectively, relative to the sum of the covalent radii.[45] In each case the strength of the back bonds contracts the surface layer inward toward the bulk. In the GaAs case, the contraction is shared across both substrate bonds $Ga_{(1)}$-$As_{(2)}$, and $(Ga)_2$-$(As)_1$. For more ionic InP, the $(In)_1(P)_2$ back bond undergoes a contraction, whereas the $(In)_2(P)_1$ back bond expands. In both cases these modifications of the bond lengths relative to bulk covalent bonding expectations occur in addition to the rotation of the top layer. Although these changes in bond length lie within the uncertainties inherent in the structure-determination methodology,[55] the use of exactly the same procedure to analyze the LEED intensities from GaAs and InP permits us a more precise comparison of the two sets of structures.

There is a moderate dependence on the number of phase shifts used in the calculation presented in Table I and the goodness of fit, R_x. The results for InP show that a six-phase-shift model improves the fits over the five-phase-shift result, but the use of a seven-phase-shift model does not significantly improve the R_x values.

TABLE IV. Comparison of best-fit epitaxical continued-layer structure (ECLS) geometries to the results of previous determinations. Symbols in the table are defined in Fig. 1 and the caption to Table I. A discussion of the comparison of our results with prior ones for InP(110) and InP(110)-$p(1\times1)$-Sb(1 ML) is given in Sec. IV of the text.

InP(110)	ω_1 (deg)	$d_{12,\perp}$ (Å)	$(In)_1$-$(P)_1$ (Å)	$(In)_1$-$(P)_2$ (Å)	$(In)_2$-$(P)_1$ (Å)	
This work	−31.1	1.88	2.52	2.49	2.55	
Chadi (Ref. 63)	−26.5	1.91	2.53	2.49	2.51	
Mailhiot, Duke, and Chadi (Ref. 64)	−31.8					
Duke (Ref. 55)	−30.0	1.92	2.54	2.46	2.59	
Meyer *et al.* (Ref. 54)	−30.4	1.79	2.48	2.47	2.44	
Choudhary *et al.* (Ref. 65)			2.43			
Choudhary *et al.* (Ref. 66)			2.45			
Sb/InP(110)	**ω_1 (deg)**	**$d_{12,\perp}$ (Å)**	**Sb-Sb (Å)**	**Sb-In (Å)**	**Sb-P (Å)**	**θ (deg)**
Covalent			2.80	2.84	2.46	95.6
This work	−3.9	2.32	2.82	2.80	2.52	94.8
Duke *et al.*, small $\Delta_{1,\perp}$ (Ref. 9)	−8.4	2.31	2.68	2.86	2.49	101.3
Duke *et al.*, large $\Delta_{1,\perp}$ (Ref. 9)	−22.8	2.11	2.84	2.81	2.07	94.0
Mailhiot, Duke, and Chadi (Ref. 6)	−15.8	1.99	2.95	2.91	1.82	89.4
Bi/InP(110)	**ω_1 (deg)**	**$d_{12,\perp}$ (Å)**	**Bi-Bi (Å)**	**Bi-In (Å)**	**Bi-P (Å)**	**θ (deg)**
Covalent			2.92	2.90	2.52	90.6
This work	−5.4	2.48	2.98	2.88	2.58	88.3

Indeed, the five-phase-shift model predicts a geometry that is very close to the converged seven-phase-shift calculation. The major difference is that the $(In)_1$-$(P)_2$ bond is more contracted in the best-fit geometry relative to the bulk nearest-neighbor distance. Each calculation reported in Tables I–III was repeated several times using a difference initial simplex on the structure search in order to test the stability of the converged results to the choice of starting condition.

Stranski-Krastanov (SK) growth is a mode of thin-film formation that is intermediate between laminar growth and three-dimensional clustering. In the SK mode, an adsorbate atom first forms a two-dimensional overlayer at coverages of less than a monolayer. Subsequent growth occurs as disordered three-dimensional clusters.

The LEED data presented here supports a SK growth mode for both Sb and Bi on InP(110). At coverages much less than one monolayer, the diffraction angular profiles for each system exhibit an energy-dependent broadening. This phenomenon has been reported previously for Sb/InP(110),[8] as well as for the similar epitaxical systems of Sb and Bi on GaAs(110),[4,38,41,43] and has been interpreted as being due to two-dimensional island growth. For idealized systems containing distributions of small-sized two-dimensional islands, an energy-dependent diffraction broadening is expected.[62] Although the local InP substrate geometry is significantly modified upon Sb or Bi adsorption, a similar phenomenon should occur when the island size is sufficiently small compared with the coherence lengths of the incident electrons, which for this study is approximately 100 Å.[40]

Trends in the LEED-intensity profiles also support a SK growth model (cf. Fig. 6). The measured LEED intensities represent an average value over the area of the surface exposed to the incident electron beam, ~ 0.01 mm^2. If the overlayer deposits as a disordered film, the effect on the diffraction intensities would be a general reduction in intensities. Conversely, compact two-dimensional island formation would cause the measured intensities to constitute an average of the overlayer and clean-surface regions. If the surface coverage is increased and the island size and concentration increases, the measured intensity profiles should gradually convert to those representing the ordered monolayer from those of the clean surface. A gradual change was observed in the individual intensity profiles at coverages below one monolayer (cf. Fig. 6). This change is consistent with two-dimensional ordered island formation. At coverages greater than 1 ML, however, no changes in the intensity profiles were observed for either Sb/InP or Bi/InP (cf. Fig. 6), although an increase in incoherent background scattering occurred. The lack of change in the intensity profiles indicates that the long-range two-dimensional order is not modified with increasing Sb or Bi coverage.

Finally, Auger and photoelectronic spectroscopy studies of Sb/InP and Bi/InP have been reported which are in agreement with a SK growth mode.[7,8] In these studies the substrate core-level transition energies and intensities were shown to support the theory of a laminar film formation in the first monolayer of coverage and three-dimensional clustering at higher coverages. A similar conclusion was made previously for the Sb/GaAs(110) system using photoemission analyses.[30,31]

Split-integral-order diffraction profiles occur at submonolayer coverages for Bi/InP(110) (cf. Figs. 8 and 9). A similar observation was reported previously for Sb/InP(110).[8] The diffraction satellites in Fig. 8 are narrow along the $[1\bar{1}0]$ direction and broad along the [001] direction. The splitting is constant over a wide range of coverage, extending from approximately 0.2 to 0.7 ML, and corresponds to a real-space periodicity of 90 ± 20 Å along the $[1\bar{1}0]$ direction. Short zigzag chains, which form along the $[1\bar{1}0]$ direction, would give rise to the splitting. At submonolayer coverages, the chains are envisioned to organize into islands laterally with respect to the chain direction. The breadth of the diffraction spot along the [001] direction indicates an irregular relative positioning of the chains.

Because the amount of diffraction-spot splitting is independent of coverage, the average chain length must increase with increasing Bi coverage. For example, at 0.5 ML the average chain length would be approximately 45 Å. This value matches the estimate of the island size of Sb on InP(110) at 0.5 ML coverage made previously using the maximum diffraction-spot-profile widths.[8] The fact that the splitting remains constant with increasing coverage indicates that the Bi atoms, and by analogy the Sb atoms, have a relatively high mobility along the $[1\bar{1}0]$ direction at room temperature.

A similar diffraction-spot splitting was observed in the LEED study of the Bi/GaAs(110) system.[40,41,43] In that case, however, the splitting is due to the formation of short chains whose length was fixed at 24 Å, independent of the coverage. The chain length was constrained by a formation of a chain vacancy as a result of a lattice mismatch between the Bi adatom and underlying GaAs(110) periodicity.[32] Such an effect does not occur for the Bi/InP system.

Generally, the "size" of the adsorbate atom is thought to play an important role in determining whether an ordered interface will form. The difference between the large atomic size of Bi relative to Sb has been used to reconcile the observation of short $[1\bar{1}0]$ Bi chains on GaAs(110) with the observation of the uniform overlayer growth for Sb on GaAs(110) in the first monolayer of coverage.[32] If the relative size of an atom is defined as the ratio of its covalent radius to the substrate lattice constant, then Sb has a relative size of 0.25 on GaAs(110) and 0.24 on InP(110), and Bi has a relative size of 0.26 on GaAs(110) and 0.25 on InP(110). Both the Sb and Bi overlayers should be better accommodated on InP(110). Furthermore, because the relative size of Sb/GaAs is identical to Bi/InP, a uniform island formation similar to that observed on Sb/GaAs should be exhibited by Bi/InP. Instead, both Sb and Bi form regular chains on InP(110) at submonolayer coverages, leading to a diffraction-spot splitting which has not been observed in any study of Sb/GaAs. Therefore atomic size alone is inadequate to explain the island formation at submonolayer coverages for all column-V/III-V (110) systems.

The chemisorption of Bi and Sb on InP(110) serves to undo the relaxation of the clean surface. The results of

multiple-scattering analysis reported in the present study indicate that of the geometries tested only the ECLS geometry (cf. Fig. 1 and Table I) is consistent with the measured LEED-intensity data. The resultant geometry is a "truncated bulk" arrangement of atoms in which the top layer of atoms consists solely of the adsorbate. In the best-fit InP(110)-$p(1\times1)$-Sb(1 ML) geometry, the In-Sb, Sb-Sb, and Sb-P bonds undergo changes of -1.4%, 0.7%, and 2.4%, respectively, with respect to nominal covalent bond lengths. The best-fit Bi/InP(110) geometry predicts a -3.4%, 2.1%, and 2.4% change in the In-Bi, Bi-Bi, and Bi-P bond lengths, respectively. Thus, in each case, the LEED results suggest that the adsorbate bonds to P undergo an expansion, and the adsorbate bonds to In a contraction, relative to covalent-bond-length expectations. There is some evidence of an expansion in the adsorbate-adsorbate bond lengths, which is particularly evident in the case of the larger Bi atom. The magnitudes of all of these phenomena lie within the uncertainties inherent in the structure-determination methodology.

Column-V adsorbates bond to a III-V (110) surface by forming a zigzag chain of atoms along the $[1\bar{1}0]$-direction bridging between similar rows of atoms in the substrate (cf. Fig. 1). The extra valence electrons of the column-V adatoms hybridize into a p^2 configuration. One measure of the completeness of the p^2 bonding is how much the in-plane bond angle θ differs from 90°. In Table IV the value of θ computed for Sb and Bi are tabulated. Generally, the best-fit values determined in this study are very close to the values predicted using only the covalent bond lengths. The θ values indicate that the Bi system, with a bond angle of 88°, is more ideally p^2 than the 95° characteristic of the Sb overlayer.

Table IV permits the comparison of our results for InP(110)-$p(1\times1)$-Sb(1 ML) both with those obtained via a previous LEED-intensity analysis[9] and with those predicted by a tight-binding total-energy calculation.[6] The earlier LEED-intensity analysis identified two local minima in both R_x and the integrated intensity R factor R_I, labeled "small $\Delta_{1,\perp}$" and "large $\Delta_{1,\perp}$" in Table IV. The prior studies were, however, unable to resolve which minimum was preferred.[9] As is evident from Table IV, the present analysis decisively favors the small-$\Delta_{1,\perp}$ minimum. Indeed, to test the stability of the large- and small-$\Delta_{1,\perp}$ (i.e., ω_1), structures, simplex searches were performed using starting geometries close to each of the two previous structures and the experimental LEED-intensity data measured in this study. In each case the search converged to the new best-fit structure reported here. Figure 11 shows that using the best-fit geometry computed here, only one structure, the small-angle case, is consistent with the experimental data. The fact that we obtain $\omega_1=-4°$ rather than $-8°$, as obtained by Duke *et al.*,[9] reflects our use solely of R_x as the best-fit figure of merit. Duke *et al.*[9] used both R_x and R_I as figures of merit. This procedure moved the best-fit value from $-4°$ to $-8°$, as evident from Fig. 4 of Ref. 9. The fact that the two procedures lead to different bond lengths results from different selections of the independent structural variables. Our simplex optimization procedure always modifies displacements normal to the surface when bond lengths are varied. Hence the effect of displacements parallel to the surface on the surface structure is not explored. Given these restrictions on the present analysis (i.e., the use of R_x alone as the best-fit figure of merit and of bond lengths alone as independent structural variables), we regard the results presented in Table IV as yielding a quantitative confirmation of the small-$\Delta_{1,\perp}$ structure reported by Duke *et al.*[9] The larger deviations from the tight-binding total-energy predictions of Mailhiot, Duke, and Chadi[6] are consequences of the short Sb-P bond length used as input to these calculations. This bond length is not known from small-molecule atomic geometries, and as discussed in Ref. 6, the uncertainty in its value introduces corresponding ones in the model predictions of the InP(110)-$p(1\times1)$-Sb(1 ML) atomic geometry.

The uncertainties inherent in the best-fit structural coordinates in Table IV may be inferred from Fig. 5 of Duke *et al.*[9] Coordinates normal to the surface are accurate to within about ±0.05 Å and those parallel to the surface to within a much larger interval, roughly ±0.2 Å. Within these uncertainties the small-$\Delta_{1,\perp}$ structure of Ref. 9 and the present results given in Table IV are equivalent.

The EOTS geometry has been proposed as a possible alternative structure to the ECLS model. Raman and some photoelectron spectroscopic studies have suggested this interpretation.[19,48,49] STM analysis[17] and tight-binding calculations[20] have not ruled out the possibility. Our attempt to fit a EOTS geometric model to the LEED data for either Sb or Bi on InP(110) failed (cf. Table III). From a chemical perspective, the EOTS geometry should be unstable to electronegative adsorption. It has been shown, however, that Sb/InP is stable to O_2 adsorption.[8] It is interesting to note that the spectroscopic argument made in support of the EOTS geometry predicts a stronger Sb and Bi bond to In than to P. The LEED results indicated in Table I suggest that the Sb-In and Bi-In bond lengths contract by 0.04 and 0.02 Å, respectively, while the Sb-P and Bi-P bond lengths expand by 0.06 Å each, relative to their covalent values. If a bond-length contraction is interpreted as a bond strengthening, the results of the LEED-intensity analysis are in agreement with the spectroscopic conclusions made above, although the LEED analysis yields a different geometry.

V. SYNOPSIS

A LEED-intensity analysis of the surface geometries of InP(110), InP(110)-$p(1\times1)$-Sb(1 ML), and InP(110)-$p(1\times1)$-Bi(1 ML) has been presented. The same experimental conditions were used for the LEED-intensity measurements and a common dynamical multiple-scattering model was used to analyze the results. Refined geometries for the InP(110) and InP(110)-$p(1\times1)$-Sb(1 ML) systems have been presented and compared to that for the InP(110)-$p(1\times1)$-Bi(1 ML) system, which is reported here for the first time, and to those for the analogous GaAs(110) systems, which were reported previously. Our results for InP(110) confirm, quantitatively, those obtained earlier by LEED-intensity analyses.[54,55] Similarly,

our results for InP(110)-$p(1\times1)$-Sb(1 ML) resolve an ambiguity between two apparently equivalent structures identified in a previous LEED-intensity analysis[9] by yielding a quantitative confirmation of the small-$\Delta_{1,\perp}$ structure emanating from this analysis. The atomic geometries of the Sb and Bi on InP(110) overlayer systems have been shown to be very similar and to be examples of the ECLS geometry. The alternative EOTS geometry was found to be inconsistent with the LEED data. The growth mode of the one-monolayer Sb and Bi films was shown to be that of Stranski and Krastanov. An unusual terracing of the overlayer into short chains running along the $[1\bar{1}0]$ direction was observed. The length of these chains varied with coverage, unlike previous observations for the Bi/GaAs(110) system. Finally, the concept of the atomic size was shown to be inadequate to explain the differences between the adsorption properties of Sb and Bi on the GaAs and InP(110) substrates.

ACKNOWLEDGMENTS

This work was supported by a grant from the National Science Foundation, Grant No. DMR-8705879, and by the National Center for Supercomputing Applications.

---

*Present address: Intel Corporation, 5200 NE Elam Young Parkway, AL3-15, Hillsboro, OR 97124.

†Present address: Gould AMI Semiconductors, Research and Development, 2300 Buckskin Road, Pocatello, ID 832001.

[1]P. Skeath, I. Lindau, C. Y. Su, and W. E. Spicer, J. Vac. Sci. Technol. **19**, 556 (1981); P. Skeath, C. Y. Su, I. Lindau, and W. E. Spicer, J. Cryst. Growth **56**, 505 (1982); P. Skeath, C. Y. Su, W. A. Harrison, I. Lindau, and W. E. Spicer, Phys. Rev. B **27**, 6246 (1983).

[2]C. B. Duke, A. Paton, W. K. Ford, A. Kahn, and J. Carelli, Phys. Rev. B **26**, 803 (1982).

[3]A. Kahn, J. Carelli, C. B. Duke, A. Paton, and W. K. Ford, J. Vac. Sci. Technol. **20**, 775 (1982).

[4]J. Carelli and A. Kahn, Surf. Sci. **116**, 380 (1982).

[5]K. Li and A. Kahn, J. Vac. Sci. Technol. A **4**, 958 (1986).

[6]C. Mailhiot, C. B. Duke, and D. J. Chadi, Phys. Rev. Lett. **53**, 2114 (1984); Phys. Rev. B **31**, 2213 (1985).

[7]C. Stringer, A. McKinely, G. Hughes, and R. H. Williams, Vacuum **33**, 597 (1983).

[8]K. Li, C. R. Bonapace, and A. Kahn, in *Proceedings of the 17th International Conference on the Physics of Semiconductors,* edited by D. J. Chadi and W. Harrison (Springer, New York, 1985), p. 129.

[9]C. B. Duke, C. Mailhiot, A. Paton, K. Li, C. Bonapace, and A. Kahn, Surf. Sci. **163**, 391 (1985).

[10]A. Tulke, M. Mattern-Klossen, and H. Lüth, Solid State Commun. **59**, 303 (1986).

[11]A. Tulke and H. Lüth, Surf. Sci. **178**, 131 (1986).

[12]P. Mårtensson, G. V. Hansson, M. Lahdeniemi, K. O. Magnusson, S. Wiklund, and J. M. Nicholls, Phys. Rev. B **33**, 7399 (1986).

[13]W. Pletschen, N. Esser, H. Münder, D. R. T. Zahn, J. Geurts, and W. Richter, Surf. Sci. **178**, 140 (1986).

[14]F. Schäffler, R. Ludeke, A. Taleb-Ibrahimi, G. Hughes, and D. Rieger, Phys. Rev. B **36**, 1328 (1987); J. Vac. Sci. Technol. B **5**, 1048 (1987).

[15]W. Drube and F. J. Himpsel, Phys. Rev. B **37**, 855 (1988).

[16]R. Cao, K. Miyano, T. Kendelewicz, I. Lindau, and W. E. Spicer, Surf. Sci. **206**, 413 (1988).

[17]P. Mårtensson and R. M. Feenstra, J. Microsc. **152**, 761 (1988); Phys. Rev. B **39**, 7744 (1989); R. M. Feenstra and P. Mårtensson, Phys. Rev. Lett. **61**, 447 (1988).

[18]C. K. Shih, R. M. Feenstra, and P. Mårtensson, J. Vac. Sci. Technol. A **8**, 3379 (1990).

[19]N. Esser, M. Reckzügel, R. Srama, U. Resch, D. R. T. Zahn, W. Richter, C. Stephens, and M. Hünermann, J. Vac. Sci. Technol. B **8**, 680 (1990).

[20]J. P. LaFemina, C. B. Duke, and C. Mailhiot, J. Vac. Sci. Technol. B **8**, 888 (1990).

[21]G. Annovi, M. G. Betti, U. del Pennino, and C. Mariani, Phys. Rev. B **41**, 11 978 (1990).

[22]F. Manghi and C. Calandra, Vacuum **41**, 693 (1990).

[23]T. J. Godin, J. P. LaFemina, and C. B. Duke, J. Vac. Sci. Technol. B **9**, 2282 (1991).

[24]T. Kendelewicz, J. C. Woicik, K. E. Miyano, P. L. Cowan, B. A. Karlin, C. F. Bouldin, P. Pianetta, and W. E. Spicer, J. Vac. Sci. Technol. B **9**, 2290 (1991).

[25]A. Yu. Mityagin, V. V. Panteleev, and L. S. Telegina, Fiz. Tverd. Tela (Leningrad) **18**, 1482 (1976) [Sov. Phys. Solid State **18**, 862 (1976)].

[26]C. B. Duke, J. Vac. Sci. Technol. A **6**, 1957 (1988).

[27]C. B. Duke, *Properties of Gallium Arsenide,* 2nd ed. (Institution of Electrical Engineers, London, 1990), pp. 418–420.

[28]C. B. Duke, *Properties of Indium Phosphide* (Institution of Electrical Engineers, London, 1991), pp. 297–298.

[29]V. F. Dvoryankin, A. A. Komarov, and V. V. Panteleev, Sov. J. Mater. **19**, 186 (1983).

[30]J. J. Joyce, J. Anderson, M. M. Nelson, C. Yu, and G. J. Lapeyre, J. Vac. Sci. Technol. A **7**, 850 (1989).

[31]J. J. Joyce, J. Anderson, M. M. Nelson, and G. J. Lapeyre, Phys. Rev. B **40**, 10 412 (1989).

[32]A. B. McLean, R. M. Feenstra, A. Taleb-Ibrahimi, and R. Ludeke, Phys. Rev. B **39**, 12 925 (1989).

[33]Y. Hu, T. J. Wagener, M. B. Jost, and J. H. Weaver, Phys. Rev. B **40**, 1146 (1989).

[34]R. M. Feenstra, P. Mårtensson, and R. Ludeke, in *Characterization of the Structure and Chemistry of Defects in Materials,* edited by B. C. Larson, M. Rühle, and D. N. Seidman, MRS Symposium Proceedings No. 138 (Materials Research Society, Pittsburgh, 1989), p. 305.

[35]R. Ludeke, A. Taleb-Ibrahimi, R. M. Feenstra, and A. B. McLean, J. Vac. Soc. Technol. B **7**, 936 (1989).

[36]A. B. McLean and F. J. Himpsel, Phys. Rev. B **40**, 8425 (1989).

[37]N. Esser, M. Hünermann, U. Resch, D. Spaltmann, J. Geurts, D. R. T. Zahn, W. Richter, and R. H. Williams, Appl. Surf. Sci. **41/42**, 169 (1989).

[38]W. K. Ford, T. Guo, S. L. Lantz, K. Wan, S.-L. Chang, C. B. Duke, and D. L. Lessor, J. Vac. Sci. Technol. B **8**, 940 (1990).

[39]T. Guo, R. E. Atkinson, and W. K. Ford, in *Proceedings of the*

Industry-University Advanced Materials Conference II, edited by R. W. Smith (Advanced Materials Institute, Denver, 1989), p. 18.

[40]T. Guo, R. E. Atkinson, and W. K. Ford, Rev. Sci. Instrum. **61**, 968 (1990).

[41]T. Guo, R. E. Atkinson, and W. K. Ford, Phys. Rev. B **41**, 5138 (1990).

[42]C. B. Duke, D. L. Lessor, T. Guo, and W. K. Ford, J. Vac. Sci. Technol. A **8**, 3412 (1990).

[43]S.-L. Chang, T. Guo, W. K. Ford, A. Bowler, and E. S. Hood, in *Atomic Scale Structure of Interfaces,* edited by R. D. Bringans, R. M. Feenstra, and J. M. Gibson, MRS Symposium Proceedings No. 159 (Materials Research Society, Pittsburgh, 1990), p. 45.

[44]T. Guo, K. J. Wan, and W. K. Ford, in *Atomic Scale Structure of Interfaces* (Ref. 43), p. 39.

[45]W. K. Ford, T. Guo, D. L. Lessor, and C. B. Duke, Phys. Rev. B **42**, 8952 (1990).

[46]M. B. Jost, T. J. Wagener, Y.-J. Yu, and J. H. Weaver, Phys. Rev. B **42**, 2937 (1990).

[47]Y. J. Hu, T. J. Wagener, M. B. Jost, and J. H. Weaver, J. Vac. Sci. Technol. B **8**, 1001 (1990).

[48]C. Stephens, D. R. T. Zahn, K. Fives, R. Cimino, W. Braun, and I. T. McGovern, J. Vac. Sci. Technol. B **8**, 674 (1990).

[49]C. Stephens, D. R. T. Zahn, R. Cimino, W. Braun, K. Fives, and I. T. McGovern, Vacuum **41**, 1021 (1990).

[50]K. E. Miyano, T. Kendelwicz, R. Cao, C. J. Spindt, I. Lindau, W. E. Spicer, and J. C. Woicik, Phys. Rev. B **42**, 3017 (1990).

[51]K. M. Choudhary, P. S. Mangat, R. Seshadri, D. Kilday, and G. Margaritondo, J. Vac. Sci. Technol. B **9**, 2294 (1991).

[52]C. M. Bertoni, C. Calandra, F. Manghi, and E. Molinari, Phys. Rev. B **27**, 1251 (1983).

[53]M. Hansen and K. Anderko, *Constitution of Binary Alloys* (McGraw-Hill, New York, 1958).

[54]R. J. Meyer, C. B. Duke, A. Paton, J. C. Tsang, J. L. Yeh, A. Kahn, and P. Mark, Phys. Rev. B **22**, 6171 (1980).

[55]C. B. Duke, in *Surface Properties of Electronic Materials,* edited by D. A. King and K. P. Woodruff (Elsevier, New York, 1988), pp. 69–118.

[56]G. E. Laramore and C. B. Duke, Phys. Rev. B **2**, 4783 (1970).

[57]C. B. Duke and C. W. Tucker, Surf. Sci. **15**, 231 (1969).

[58]W. K. Ford, C. B. Duke, and A. Paton, Surf. Sci. **112**, 195 (1985).

[59]R. J. Meyer, C. B. Duke, and A. Paton, Surf. Sci. **97**, 512 (1980).

[60]J. L. Beeby, J. Phys. C **1**, 82 (1968).

[61]E. Zanazzi and F. Jona, Surf. Sci. **62**, 61 (1977).

[62]M. G. Lagally, in *Methods of Experimental Physics,* edited by R. L. Park and M. G. Legally (Academic, New York, 1985), Vol. 22, pp. 237–298; M. Henzeler, in *Electron Spectroscopy for Surface Analysis,* edited by H. Ibach (Springer, Berlin, 1977), Chap. 4.

[63]D. J. Chadi, Phys. Rev. B **19**, 2074 (1979).

[64]C. Mailhiot, C. B. Duke, and D. J. Chadi, Surf. Sci. **149**, 366 (1985).

[65]K. M. Choudhary, P. S. Mangat, A. E. Miller, D. Kilday, A. Filipponi, and G. Margaritondo, Phys. Rev. B **38**, 1566 (1988).

[66]K. M. Choudhary, P. S. Mangat, H. I. Starnberg, Z. Hurych, D. Kilday, and P. Soukiassian, Phys. Rev. B **39**, 759 (1989).

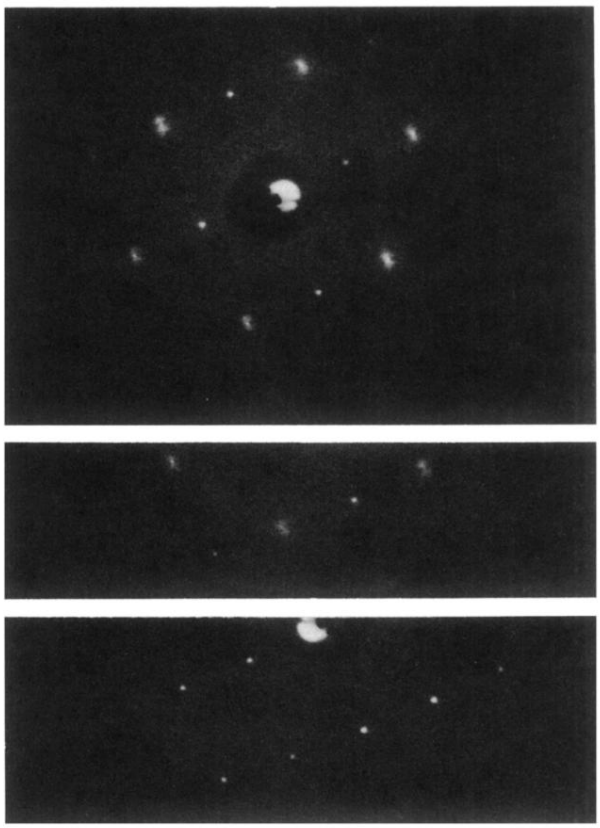

FIG. 8. LEED patterns at 69 eV for Bi/InP(110) for (a) 0.36 ML, (b) 0.55 ML, and (c) 0.96 ML.